

## Investigation and optimization of the magnetic field configuration in high-power impulse magnetron sputtering

This content has been downloaded from IOPscience. Please scroll down to see the full text.

2013 Plasma Sources Sci. Technol. 22 045012

(<http://iopscience.iop.org/0963-0252/22/4/045012>)

View [the table of contents for this issue](#), or go to the [journal homepage](#) for more

Download details:

IP Address: 130.126.32.13

This content was downloaded on 04/06/2014 at 18:26

Please note that [terms and conditions apply](#).

# Investigation and optimization of the magnetic field configuration in high-power impulse magnetron sputtering

He Yu<sup>1,2</sup>, Liang Meng<sup>1</sup>, Matthew M Szott<sup>1</sup>, Jake T McLain<sup>1</sup>, Tae S Cho<sup>1</sup>  
and David N Ruzic<sup>1</sup>

<sup>1</sup> Center for Plasma Material Interactions, Department of Nuclear Plasma and Radiological Engineering, University of Illinois at Urbana-Champaign, Urbana, IL 61801, USA

<sup>2</sup> State Key Laboratory of Electronic Thin Films and Integrated Devices, School of Optoelectronic Information, University of Electronic Science and Technology of China, Chengdu 610054, People's Republic of China

E-mail: [yuheuiuc@gmail.com](mailto:yuheuiuc@gmail.com)

Received 3 April 2013

Published 5 July 2013

Online at [stacks.iop.org/PSST/22/045012](http://stacks.iop.org/PSST/22/045012)

## Abstract

An effort to optimize the magnetic field configuration specifically for high-power impulse magnetron sputtering (HiPIMS) was made. Magnetic field configurations with different field strengths, race track widths and race track patterns were designed using COMSOL. Their influence on HiPIMS plasma properties was investigated using a 36 cm diameter copper target. The  $I$ - $V$  discharge characteristics were measured. The temporal evolution of electron temperature ( $T_e$ ) and density ( $n_e$ ) was studied employing a triple Langmuir probe, which was also scanned in the whole discharge region to characterize the plasma distribution and transport. Based on the studies, a closed path for electrons to drift along was still essential in HiPIMS in order to efficiently confine electrons and achieve a high pulse current. Very dense plasmas ( $10^{19}$ – $10^{20}$  m<sup>-3</sup>) were generated in front of the race tracks during the pulse, and expanded downstream afterwards. As the magnetic field strength increased from 200 to 800 G, the expansion became faster and less isotropic, i.e. more directional toward the substrate. The electric potential distribution accounted for these effects. Varied race track widths and patterns altered the plasma distribution from the target to the substrate. A spiral-shaped magnetic field design was able to produce superior plasma uniformity on the substrate in addition to improved target utilization.

(Some figures may appear in colour only in the online journal)

## 1. Introduction

Magnetron sputtering (MS) has been used in a variety of industrial applications such as hard coatings, low friction coatings and coatings with specific optical or electrical properties [1–7]. A magnetron is designed to magnetically enhance and confine the plasma close to the cathode (the target). The orthogonal electric ( $E$ ) and magnetic ( $B$ ) fields result in a classic  $E \times B$  drift for electrons. The drifting paths form closed loops so that electrons are constrained, circulating many times in the near vicinity of the target. The enhanced plasma density allows for a few per cent of the sputtered atoms to be ionized. An interest to further increase the ionization,

initially driven by the need to deposit metal layers and diffusion barriers in high aspect ratio interconnects during integrated circuit (IC) fabrication, led to the development of ionized physical vapor deposition (iPVD) [2–5, 8]. The methods to implement iPVD include supplementary plasma enhancement [7, 9], hollow cathode magnetron [5, 10], high-power impulse magnetron sputtering (HiPIMS), etc. HiPIMS was introduced by Kouznetsov *et al* [11] and has been extensively studied ever since [12–14]. It is featured with very high peak power on the target. Dense plasmas of  $10^{19}$ – $10^{20}$  m<sup>-3</sup> in front of the target are consequently achieved to produce a high degree of ionization of the sputtered material [15–17].

Magnetic field design is important in dcMS to affect the plasma and the film deposition [1, 18–20]. The  $B$  field determines the efficiency of plasma confinement and thus the sputtering rate. The  $B$  field profile on the target surface defines the drifting path of electrons and the resultant erosion pattern such as the so-called ‘race track’ on the target. It is generally desirable to have a full face target erosion to control the re-deposition and to extend the target lifetime. For a sputtering process, it is usually critical to have uniform downstream plasmas and deposition rates, which are affected by the race track pattern as well as the degree of unbalancing in the magnetic field [1, 18]. The magnetic field configuration has to be carefully customized and combined with magnet pack rotation or scanning to optimize the magnetron performance, especially for deposition on large substrates. However, the optimization of magnetic field has been largely overlooked in HiPIMS. In most cases, rotating or scanning magnets designed for dcMS are commonly used. It is known that the HiPIMS discharge mechanisms are unique and complex. The behaviors of the pulsed plasma including the plasma ignition, plasma growth and the downstream plasma release are different from those in dcMS. The influence of the magnetic field configuration on these processes is undoubtedly important, but has not been systematically studied except for a few discussions regarding the magnetic field deformation in HiPIMS [21] or the effect of magnetic field strength in modulated pulsed power MS [22].

In this study, magnetic field configurations of different  $B$  field strengths, race track widths and race track patterns were designed using COMSOL and then created using a fully adjustable magnet pack. The HiPIMS discharge currents of these configurations in a large magnetron system were measured. A three-dimensional (3D) scanning triple Langmuir probe was used to measure the distribution of plasma parameters such as the electron temperature  $T_e$ , electron density  $n_e$  and floating potential  $V_f$  as time evolved. The effects of magnetic field on the plasma generation and transport processes were discussed. Special designs such as spiral-shaped race tracks were attempted to achieve both good target utilization and uniform downstream plasma distribution even without the assistance of magnet rotation.

## 2. Experimental setup

A special magnet pack was designed to allow adjusting the positions of magnets, as shown in figure 1. Magnetic field configurations of desired strength, race track pattern and degree of unbalancing could be created. COMSOL was used to assist the magnetic field design by calculating the magnetic flux intensities in the 3D discharge space for any proposed arrangement of magnets.  $B_{||}$ , as the component parallel to the target, was determined on the target surface. Its maximum value was used here to represent the magnetic field strength. The shape of  $B_{||}$  resembled the probable shape of the race track, which provided a good method for the race track pattern design. The COMSOL calculation was verified by comparing with the experimental magnetic field measurement.

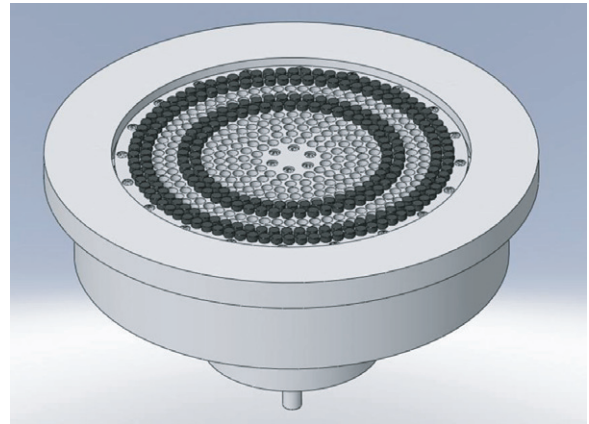
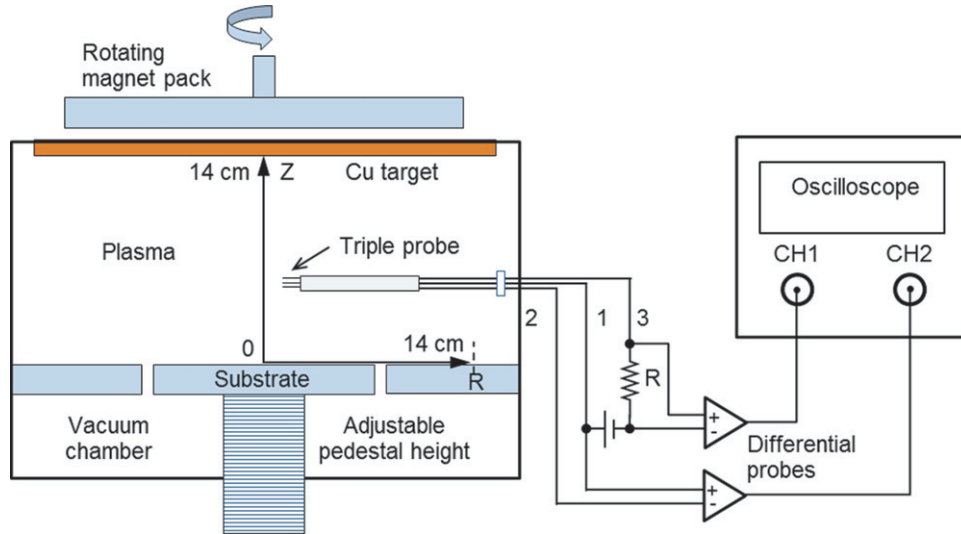


Figure 1. Specially designed adjustable magnet pack.

The experiments were performed in a commercial MRC GALAXY planar magnetron system with a 36 cm diameter copper target. The rotatable magnet pack was mounted behind the target. The schematic diagram of the chamber can be seen in figure 2. The distance between the substrate and the target was kept at 14 cm. A turbo pump was equipped to achieve a base pressure of  $5 \times 10^{-4}$  Pa. Pure argon (Ar) gas was supplied, with the working pressure typically kept at 0.67 Pa unless noted. The pressure was monitored with a capacitance manometer. The Cu target was powered with a Huettinger TruPlasma Highpulse 4002 dc generator during HiPIMS discharges while being water-cooled. The plasma generator charges its capacitor to a voltage of 500–2000 V and outputs pulses of 1–200  $\mu$ s long. A peak current up to 1 kA is allowed. The repetition frequency of pulsing is between 1 and 200 Hz. The charging voltage  $V_{ch}$ , the pulse on-time  $t_p$  and the repetition frequency  $f$  are the basic pulsing parameters. In the following sections, a set of discharge parameters is usually written in the form 800 V, 50  $\mu$ s, 100 Hz, 0.67 Pa without specifically mentioning the parameter names. The waveforms of the pulse voltage and current were measured using a high-voltage probe and a current monitor, respectively.

A triple Langmuir probe (TLP) was used for time-resolved diagnostics of the pulsed plasma. It is a simple and well-studied technique allowing instantaneous direct display of  $T_e$  and  $n_e$  [23], and was found to be very useful for pulsed plasma studies [24, 25]. The electrical setup of the triple Langmuir probe is illustrated in figure 2. More details of the TLP measurements were described in a previous paper [26]. A fixed bias ( $V_{13}$ ) of about 55 V was applied between probes 1 and 3 with a battery pack. With this bias, significantly greater than the typical  $T_e$ , ion saturation currents were collected. Probe 2 was electrically floating in the plasma discharge. All three probe tips were tungsten wires of diameter 0.25 mm and length 8.8 mm, separated by 4.0 mm. Two differential probes were used to measure  $V_{12}$  and the potential drop  $V_{34}$  across a resistor. The electron density and temperature can then be calculated using equations (1) and (2). In this study, the triple probe was configured to be capable of scanning the discharge region radially from  $R = 0$  (the central axis) to  $R = 14$  cm (near the chamber wall) and vertically between  $Z = 1$  cm



**Figure 2.** Schematic diagram of the planar magnetron with a triple Langmuir probe system.

(near the substrate) and  $Z = 13$  cm (near the target). The 3D measurements were used to study the plasma distribution and the involved plasma transport mechanism.

$$\frac{1}{2} = \frac{1 - \exp\left(-\frac{eV_{12}}{kT_e}\right)}{1 - \exp\left(-\frac{eV_{13}}{kT_e}\right)} \quad (1)$$

$$\frac{V_{34}}{R} = \exp\left(-\frac{1}{2}\right) A e n_e \sqrt{\frac{kT_e}{M}} \quad (2)$$

It should be noted, however, that the triple Langmuir probe theory is based on the assumption of a Maxwellian electron energy distribution function (EEDF). A deviation from the Maxwellian distribution, e.g. a high electron energy tail, can lead to an overestimation of  $T_e$  (or the effective electron temperature as a more accurate term to use here). Different research groups have reported that the pulsed discharge produces high-energy electrons initially, which quickly (within 10–20  $\mu$ s) evolve into a Druyvesteyn [27], bi-Maxwellian [28] or Maxwellian [29] distribution due to frequent ionization collisions and Coulomb collisions given a substantially high plasma density. There is a foreseeable error in the estimation of  $T_e$  during the initial stage of the discharge due to the large high-energy electron population. This period of the discharge is not the main focus of this study though. In the following part of the pulse and the off-time, the EEDF can be assumed to be approximately Maxwellian based on the fact that the determined  $T_e$  is typically lower than 4 eV (as shown in a later section), indicating an effective relaxation of the hot electrons. In addition, the EEDF has been reported to be truncated at energies of 4–7 eV [27, 28], so the overestimation of  $T_e$  due to the high electron energy tail should be small. With  $n_e$  only weakly depending on  $T_e$  ( $n_e \propto T_e^{-1/2}$ ), the error of calculated  $n_e$  induced by the error in  $T_e$  determination is less significant. Nevertheless, the triple Langmuir probe data were always interpreted with caution.

### 3. Results and discussion

#### 3.1. Magnetic field designs

**3.1.1. Single-ring race track with different strengths.** Configurations with different magnetic field strengths were first designed using COMSOL. Two rows of magnets were kept at the same distance to produce a simple circular shape of race track, as illustrated in figure 3. The numbers of magnets were varied in COMSOL to achieve the desired  $B_{||}$  on the target surface, i.e. maximum at 200 G, 500 G and 800 G, respectively. Such simulation results of the  $B$  field were calibrated with the experimental measurements using a magnetometer. The three configurations will be referred to as ‘200 G’, ‘500 G’ and ‘800 G’ in this paper.

**3.1.2. Single-ring race track with different widths.** Designs were then made to change the race track width while keeping a similar maximum  $B_{||}$ . The 500 G configuration was used as a baseline. By moving the inner circle of magnets further inward and adjusting the number density of the magnets, the maximum  $B_{||}$  was maintained at about 500 G. Meanwhile, the strong field region (e.g. of  $B_{||}$  greater than 200 G) spanned about twice as wide as that in the 500 G baseline configuration, as shown in figure 3(d). A wider race track was indeed created as confirmed from the subsequent observance of the discharge plasma. This field configuration is later referred to as ‘500 G-wide’.

**3.1.3. Configurations of varied race track coverage.** For better target utilization and better deposition uniformity, more evenly distributed race tracks on the target were desired. Figure 4 shows three designs of magnet arrangements and their corresponding magnetic field distributions. One design (figure 4(a)) had many groups of magnets across the whole surface with polarities opposite to the adjacent groups. The resulting  $B_{||}$  at the target surface formed a number of circles instead of a single ring as seen in the above configurations. The behavior of electrons at the connection point of two



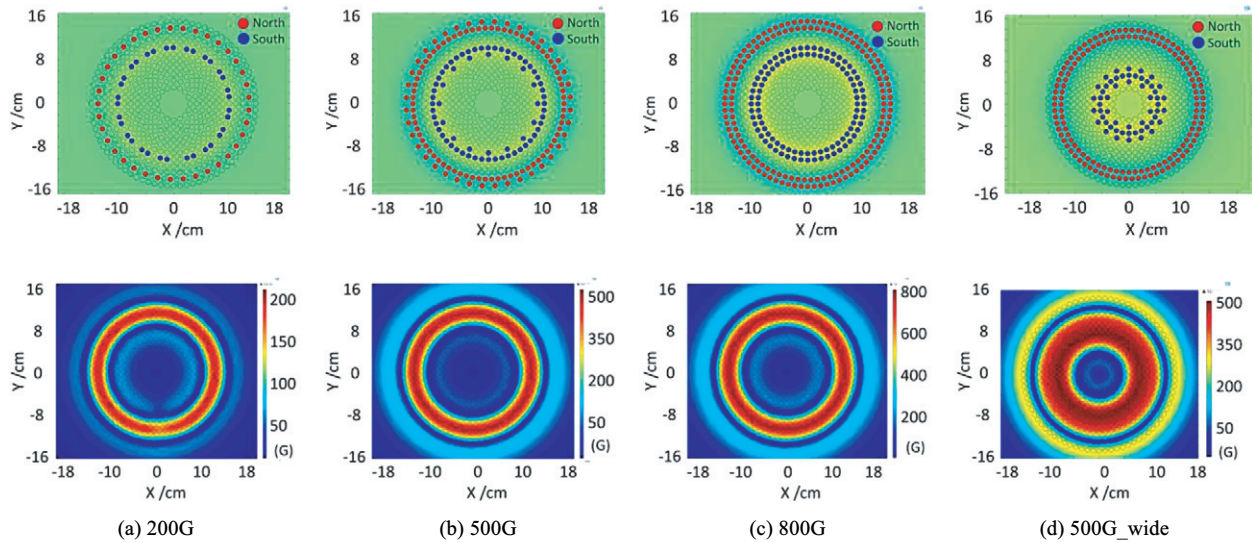


**Figure 3.** Magnet arrangements (top row) and the corresponding  $B_{\parallel}$  on the target surface (bottom row) in different configurations: (a) 200 G, (b) 500 G, (c) 800 G and (d) 500 G\_wide.

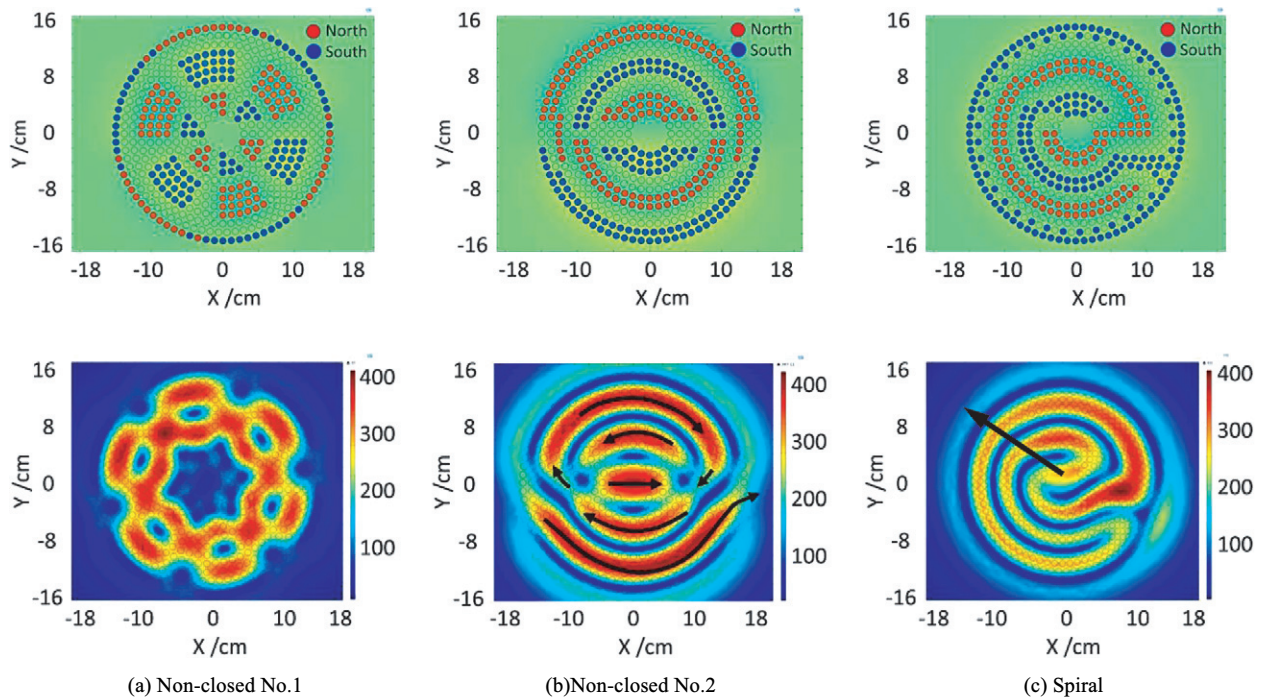


**Figure 4.** Magnet configurations with different race track shapes: (a) Non-closed No.1, (b) Non-closed No.2 and (c) Spiral. To avoid confusion, the arrow in (b) indicates the electron drift direction, while the arrow in (c) shows the radial orientation of 3D triple probe measurement, as described in the following section.

neighboring circles was to be studied, i.e. whether they stay drifting in the same circle or hop from one circle to the next or escape from confinement. Figure 4(b) shows another design, which basically has three loops of magnets, but each of them is divided into halves with opposite polarities. One of the obvious benefits of this design was the capability of sputtering the center of the target. In the above two configurations magnet polarities were switched at multiple points, forming magnetic cusps and likely non-closed race tracks. The two configurations were named ‘Non-closed No.1’ and ‘Non-closed No.2’ respectively. The third configuration (figure 4(c)) had a continuous race track using a complete outer circle.

The spiral profile of magnets resulted in a large and relatively uniform coverage of race track on the target including the center.

### 3.2. Discharge characteristics

The pulse discharge  $I$ – $V$  characteristics were studied. A high pulse current is usually favored, not only to increase the deposition rate but also to achieve unique features of HiPIMS such as the self-sputtering effect and high ionization fraction. In a typical configuration of 500 G, as in figure 3(b), the capacitor bank was charged to 700–1000 V. Other discharge

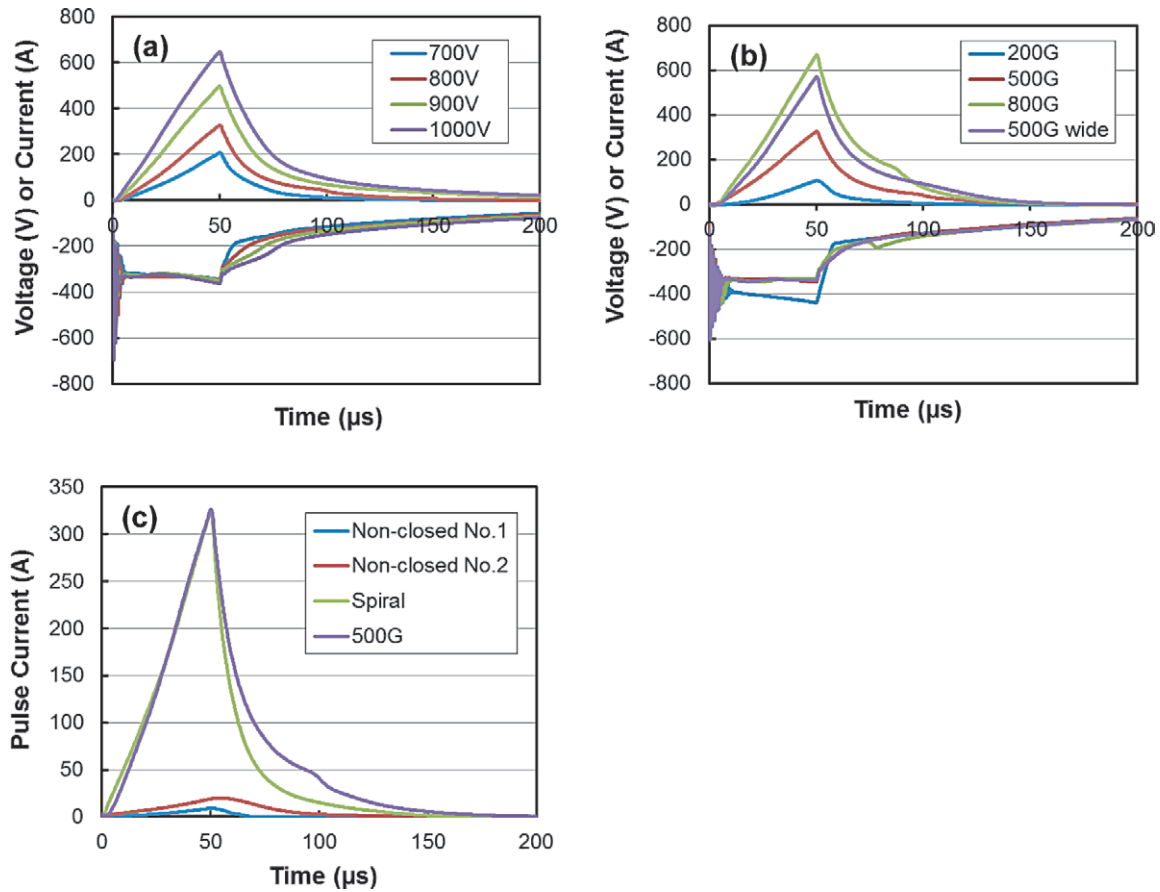


**Figure 5.** Discharge  $I$ – $V$  characteristics of different configurations. (a) Typical  $I$ – $V$  characteristics for 500 G configuration at varied charging voltage. Recipe was 800–1000 V, 50  $\mu$ s, 100 Hz, 0.67 Pa. (b)  $I$ – $V$  characteristics for 200 G, 500 G, 800 G and 500 G\_wide configurations. Recipe was 800 V, 50  $\mu$ s, 100 Hz, 0.67 Pa. (c) Pulse currents for non-closed and spiral configurations as compared with the 500 G one. Recipes were 1000 V, 50  $\mu$ s, 100 Hz, 1.33 Pa for Non-closed No.1, and 800 V, 50  $\mu$ s, 100 Hz, 0.67 Pa for others.

parameters were  $t_p = 50 \mu$ s,  $f = 100$  Hz and  $p = 0.67$  Pa. The pulse voltage on the cathode was seen to drop from the charging voltage, within several microseconds into the pulse, to a similar level of about  $-330$  V (figure 5(a)). This voltage level was determined by the impedance of the power supply, the connections to the discharge and the properties of the gas discharge itself [2]. The pulse peak current increased accordingly from 200 to 650 A. It is believed that the current ramping rate was determined by the pulse voltage during ignition. Using a recipe of higher  $V_{ch}$ , a higher voltage on the cathode initially provided each secondary electron with a higher energy to generate more electron–ion pairs and then build up a denser plasma. Given the ionization rate is directly proportional to the electron density, a greater current ramping rate was maintained even after the voltage on the cathode dropped to a similar level as in the other recipes.

The influences of magnetic field strength and race track width on discharge characteristics were then examined. The discharge parameters were kept the same as 800 V, 50  $\mu$ s, 100 Hz and 0.67 Pa. Figure 5(b) shows that by increasing the  $B_{||}$  maximum on the target surface from 200 to 800 G (figures 3(a)–(c)), a higher current was generated. It was attributed to an enhanced electron confinement and thus a more intense plasma accumulated near the race track. The increased race track width using the ‘500 G\_wide’ design (figure 3(d)) led

to a higher pulse current than 500 G. The results were expected since the erosion area was almost twice as large.

The pulse current using a non-closed race track and spiral designs are shown in figure 5(c). The ‘Non-closed No.1’ configuration had a very weak plasma. Even by using a recipe of higher charging voltage and higher pressure (1000 V, 50  $\mu$ s, 100 Hz and 1.33 Pa), the peak pulse current was less than 10 A. The pulse voltage was much higher, i.e. between 500 and 700 V (not shown here). Also, the plasma was seen to distribute in incomplete loops with no obvious connection in between, unlike the profile of touching circles in the magnetic field simulation in figure 4(a). Several factors are believed to cause the inefficient electron confinement, and consequently low plasma density and small current. The overall  $B$  field was weak, with a strong  $B_{||}$  merely localized in small regions. The  $\mathbf{E} \times \mathbf{B}$  drift of electrons could be interrupted where a magnetic cusp was formed, likely causing electrons to be driven away from the cathode and to be lost. Electrons could also leak out where magnet polarities switched in the outer circle. The ‘Non-closed No.2’ configuration generated higher currents than No.1, up to 20 A using the recipe of 800 V, 50  $\mu$ s, 100 Hz and 0.67 Pa. The pulsed voltage was between 400 and 600 V. The  $\mathbf{E} \times \mathbf{B}$  drift direction was drawn in the  $B_{||}$  mapping in figure 4(b). The bottom race track had an obvious leak to the right, while the above race tracks roughly formed

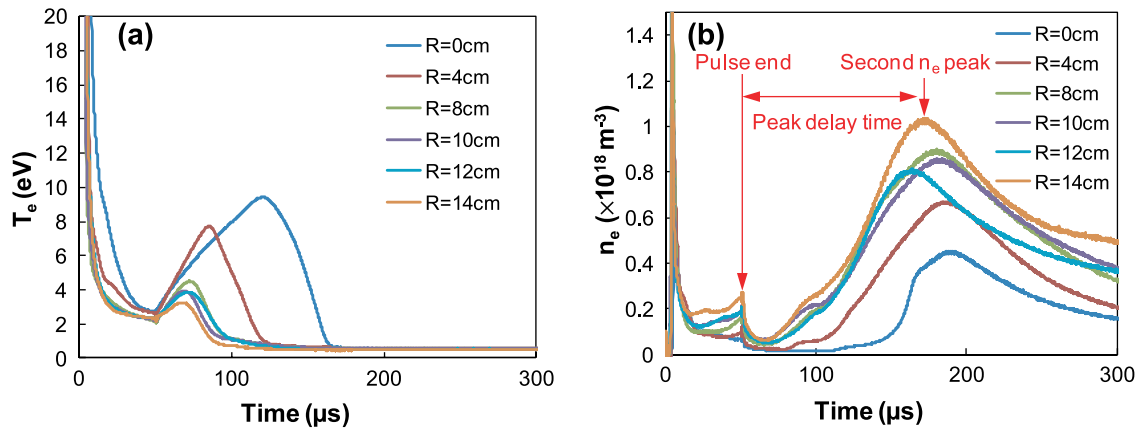


**Figure 6.** Temporal behavior of HiPIMS plasma parameters: (a)  $T_e$  and (b)  $n_e$  in the 500 G configuration, at different radial locations. The peaks seen in  $T_e$  between 50  $\mu\text{s}$  and about 160  $\mu\text{s}$  (shaded area) were artificial, which also led to an underestimation of  $n_e$  in the same period.

a closed path despite a number of potential leaking points due to weak  $B_{\parallel}$ . This is consistent with the erosion pattern on the target, displaying a weakly sputtered bottom race track with a leaking tail and more heavily sputtered race tracks in the upper part. Finally, the spiral design was tested. It was able to generate a pulse current as high as in the 500 G configuration with a similar cathode voltage. And the plasma followed the designed pattern in figure 4(c), quite uniformly distributed on the whole surface. From the study of these configurations, it can be concluded that a closed path for electrons to drift along is still essential in HiPIMS.

### 3.3. Triple Langmuir probe measurement

**3.3.1. Example of triple probe analysis.** A triple Langmuir probe was used to study the evolution and 3D distribution of plasma parameters, electron temperature  $T_e$  and density  $n_e$  in different magnet configurations. The same discharge parameters of 800 V, 50  $\mu\text{s}$ , 100 Hz and 0.67 Pa were used for the purpose of comparison. Figure 6 shows an example of analyzed  $T_e$  and  $n_e$  in the 500 G configuration. Measurements were conducted at different radial positions at a height of 1 cm above the substrate.  $T_e$  was observed to be very high at the beginning. There were considerable errors in the  $T_e$  calculation due to the non-Maxwellian distribution, but their overall high values were expected from a burst of hot electrons accelerated by the rapidly advancing cathode sheath [30]. A spike of  $n_e$  in this initial stage might be caused by the very high electron energies of several hundred eV even though the electron density was actually low. Then  $T_e$  kept decreasing to between 2 and 3 eV during the pulse, while  $n_e$  gradually increased. The peaks of  $T_e$  between 50  $\mu\text{s}$  and about 160  $\mu\text{s}$  were artificial because the plasma was too weak in the meanwhile so that  $V_{12}$  tended to return to the value of about a half of  $V_{13}$ , as in the case of no plasma present. This might cause an underestimation of  $n_e$  by a factor of 2–4. But it should not change the overall trend that  $n_e$  dropped after the pulse ended at 50  $\mu\text{s}$  and soon went up again to form a high second peak. This peak was from the plasma expansion out of the magnetic confinement region. It was also noticed that at different radial positions, the magnitude and the arrival time of this peak varied. Here, the

time interval between the pulse end and the peak arrival time is defined as the peak delay time, as illustrated in figure 6(b). To understand the mechanisms involved in the plasma expansion, a 3D characterization of the plasma expansion peaks was performed.

The second peak  $n_e$  and the peak delay time were measured at different scanned positions, as shown in figure 7. The triple probe was moved from near the substrate ( $Z = 1$  cm) to near the target ( $Z = 13$  cm), as well as from the chamber center line ( $R = 0$ ) to close to the chamber wall ( $R = 14$  cm). The highest peak  $n_e$  of  $5.4 \times 10^{19} \text{ m}^{-3}$  was at  $R = 10$  cm,  $Z = 13$  cm, reflecting the race track position. This very dense plasma is expected to produce a highly ionized metal flux and induce the self-sputtering effect. The lowest  $n_e$  ( $3.7 \times 10^{17} \text{ m}^{-3}$ ) was found to be near the center of the target, implying it was very difficult for the plasma to diffuse laterally, and the plasma distribution was extremely non-uniform near the target. As the plasma expanded from the target towards the substrate, the peak  $n_e$  rapidly decreased while the distribution in the same plane became more leveled.

Figure 7(b) displays the peak delay time at varied locations. The expansion peaks at  $R = 8, 10$  cm and box  $Z = 13$  cm appeared only a few  $\mu\text{s}$  after the pulse ended, meaning that the density started to decrease immediately. The farther the distance from the race track, the longer it took for the expansion peak to appear. About 150  $\mu\text{s}$  was needed for the expansion plasma peak to reach the substrate. It should be noted that after the plasma density peak appeared, the plasma remained for a long period before completely fading away. It is thus important to have a long enough off-time between pulses to ensure the plasma including ion species can reach the substrate.

**3.3.2. Effect of magnetic field strength.** 3D scanning triple Langmuir probe measurements were used to study the 200 G, 500 G and 800 G configurations, especially regarding the plasma transport mechanisms. Using the same method described above, the information of the expanding plasma such as the peak density and peak delay time at various positions was extracted. Instead of a line plot like figure 7, contour plots of these two parameters in the  $R$ – $Z$  plane are used to visualize their distributions. Figures 8(a)–(c) show the mapping of



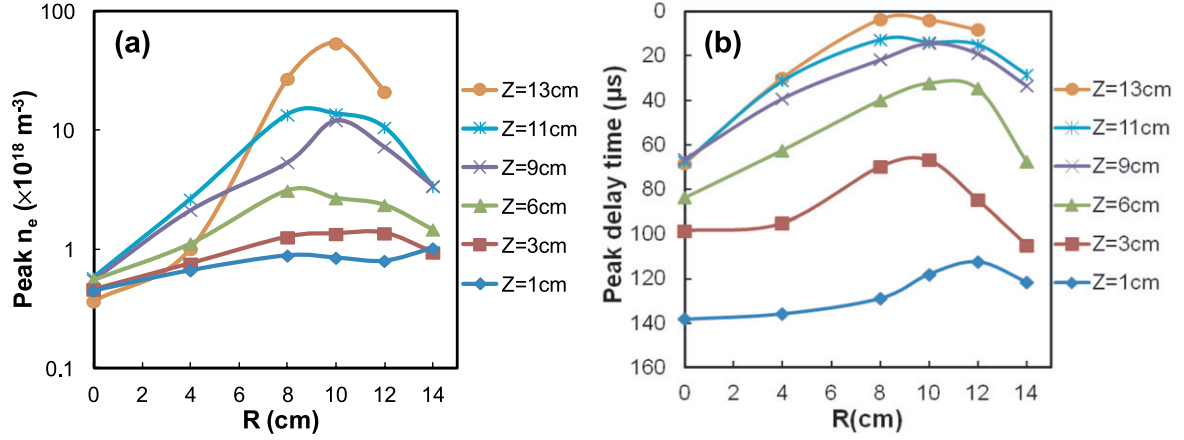


**Figure 7.** (a) Peak  $n_e$  of the expansion plasma and (b) the peak delay time after the pulse in the 500 G configuration.

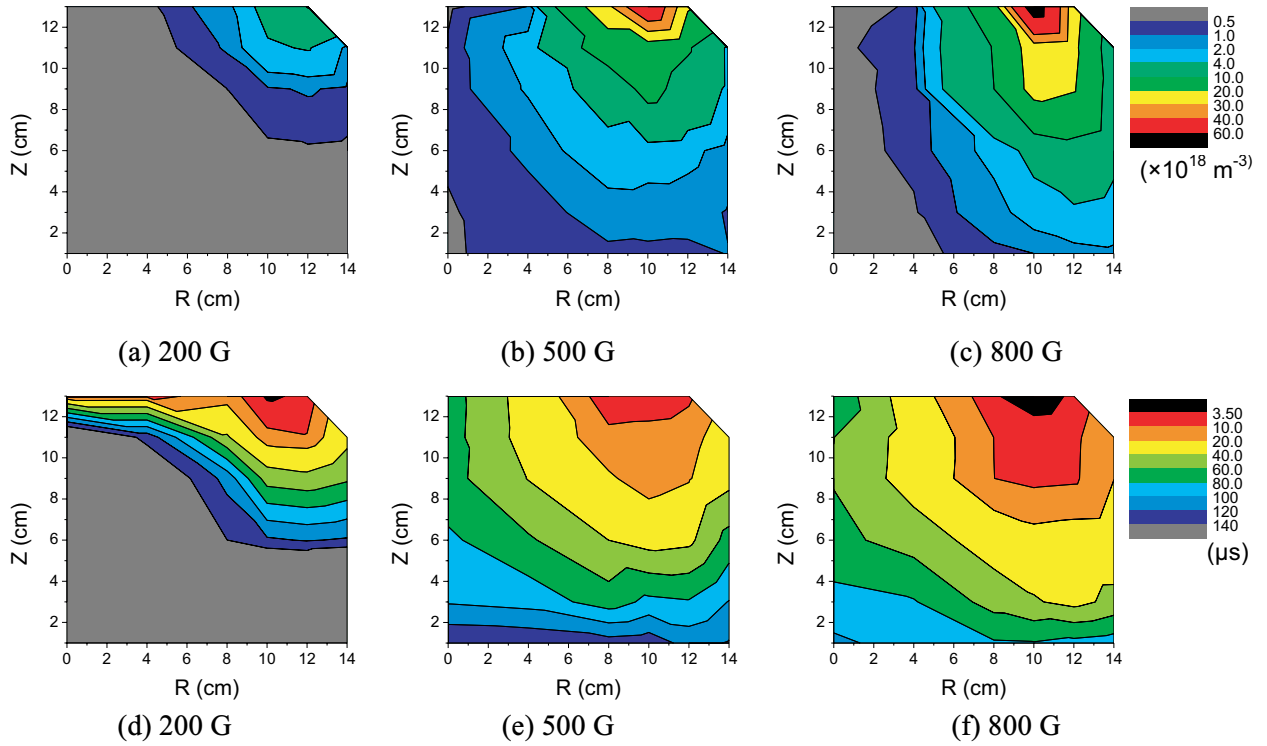


**Figure 8.** Peak  $n_e$  and the corresponding peak delay time versus various magnetic field strengths (200–800 G), (a)–(c) peak density of the expanding plasma, (d)–(f) delay time of the expansion peak.

peak  $n_e$  of the expansion plasma in the 200 G, 500 G 800 G configurations, respectively. In all three cases, peak  $n_e$  near the target reflected the ring shape of the race track. The higher the magnetic field strength, the denser the plasma. A closer look at the figures revealed that as the  $B$  field strength increased from 200 to 800 G, the expansion changed from being nearly isotropic to being more directional toward the substrate. In fact, as a result of the more directional expansion in the 800 G configuration, the peak densities around the center axis of the chamber were overall very low, even lower than those in the 500 G configuration. From figures 8(d)–(f) of the peak delay time, it can be seen that a stronger  $B$  field led to a faster expansion.

In a magnetron plasma, electrons are confined by the magnetic field via the  $\mathbf{E} \times \mathbf{B}$  drift and the diamagnetic drift

[31]. The corresponding drift velocities,  $\mathbf{u}_E$  and  $\mathbf{u}_D$ , are perpendicular to the field and the density gradients. Despite the magnetic confinement, electrons still move across the magnetic field due to drifting in the presence of the electric field and diffusion. Both contribute to  $\mathbf{u}_\perp$ , the flux velocity perpendicular to  $B_\parallel$ , as the first and second terms on the rhs of equation (3).  $\mu_\perp$  and  $D_\perp$  are the mobility and diffusion constants perpendicular to the magnetic field,  $n$  is the density and  $\mathbf{E}$  is the electric field. The last term of equation (3) describes the  $\mathbf{E} \times \mathbf{B}$  drift and the diamagnetic drift. The diffusion is strongly retarded by the magnetic field. As can be seen in equation (3),  $D_\perp$  is smaller than the diffusion coefficient without a magnetic field,  $D$ , by a factor of  $1 + (\omega_c \tau_m)^2$ . Here  $\omega_c$  is the gyration frequency and  $\tau_m \equiv \frac{1}{\nu_m}$  ( $\nu_m$  is the momentum transfer frequency),  $\bar{r}_c$  is the mean gyroradius, which is



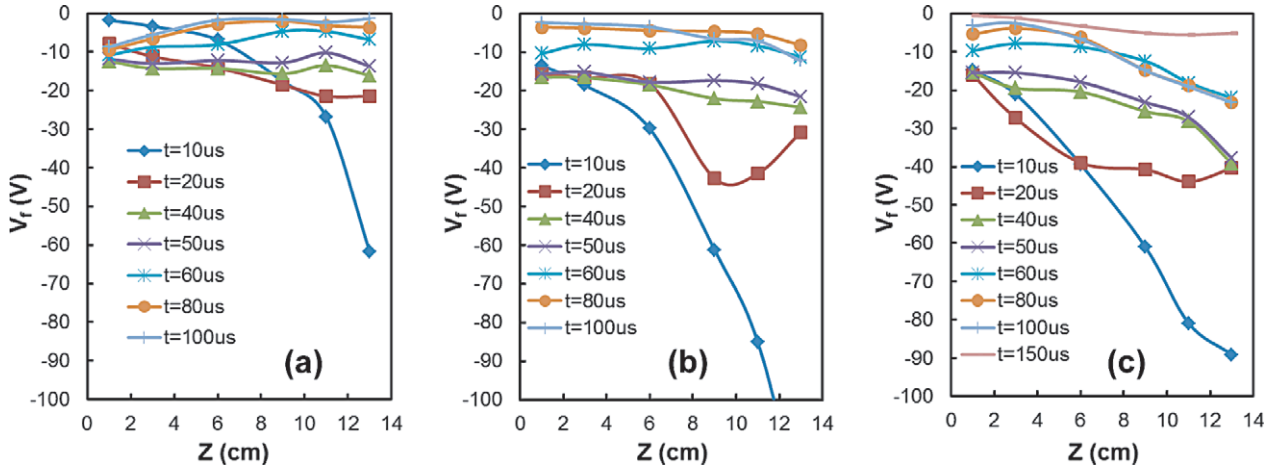


**Figure 9.** Evolution of plasma floating potential at varied  $Z$  positions ( $R = 10$  cm) in (a) 200 G, (b) 500 G and (c) 800 G configurations.

inversely proportional to  $B$ . A higher magnetic field thus has a lower diffusion coefficient to build up a higher density plasma during the discharge. It should be mentioned that non-classical diffusion has been observed in HiPIMS so that the effective collision time for electrons is much shorter and has a weaker dependence on the magnetic field strength [21, 32]. This mechanism leads to an enhanced cross- $B$  diffusion but does not explain the faster expansion in a stronger  $B$  field configuration:

$$u_{\perp} = \pm \mu_{\perp} E - D_{\perp} \frac{\nabla n}{n} + \frac{u_E + u_D}{1 + (\omega_c \tau_m)^{-2}} \quad (3)$$

$$D_{\perp} = \frac{D}{1 + (\omega_c \tau_m)^2} = \frac{\pi}{8} \bar{r}_c^2 v_m \quad (4)$$

For drifting in the electric field, the potential distribution inside the chamber should be known. The floating potentials  $V_f$  were therefore measured in all three configurations. Figure 9 shows the value of  $V_f$  from  $Z = 13$  cm to  $Z = 1$  cm below the race track ( $R = 10$  cm). Unlike in an equilibrium dc plasma where the potential difference in the presheath and in the bulk plasma is small, a very large potential drop existed along the  $Z$  direction at the beginning of the pulse ( $t = 10 \mu\text{s}$ ). As time evolved, this potential drop gradually decreased and eventually a nearly flat potential was established between  $Z = 13$  cm and  $Z = 1$  cm. The time needed for this to occur was seen to depend on the magnetic field strength, about  $40 \mu\text{s}$  in the 200 G configuration, about  $60 \mu\text{s}$  in the 500 G and more than  $150 \mu\text{s}$  in the 800 G configuration. At the pulse end, the potential differences between  $Z = 13$  cm and  $Z = 1$  cm were  $-2$ ,  $-6$  and  $-22$  V. The higher electric field in the 800 G configuration then prompted the drifting and increased the expansion speed. In contrast, the drifting in the 200 G case was less significant, and diffusion was the dominant process to result in a more isotropic expansion. The magnetic field itself is another factor to likely affect the expansion direction. For the plasma to move out of the race track region, it had to diffuse across the magnetic field, either laterally in the radial direction or in the axial direction. Magnetic field mapping showed that  $B_{\parallel}$  rapidly decreases when moving away from the target, while moving in the radial direction the magnetic field becomes stronger

because of being closer to the magnets. So in the 800 G field, it was relatively easier for the plasma to diffuse axially, while almost prohibited to move in the radial direction because of the even higher  $B$  field. This is a less significant factor for the 200 G configuration, since the overall weak  $B$  field still allowed plasma diffusion in all directions.

**3.3.3. Optimization of the plasma uniformity.** In single-ring-shaped magnetron configurations, the plasma densities near the target were significantly higher right below the race track than at the center. Although the profile was gradually washed out while approaching the substrate by scattering, a certain degree of plasma non-uniformity remained to present a concern for actual deposition processes. The capability of a magnetron configuration to even out the plasma distribution in the near vicinity of the target would be advantageous. The 500 G<sub>wide</sub> configuration was shown to benefit the target utilization. A triple Langmuir probe was then used to map the plasma distribution. Figures 10(a) and (b) compare the peak  $n_e$  and the peak delay time in the 500 G and 500 G<sub>wide</sub> configurations. A higher peak  $n_e$  was obtained near the race track, consistent with the higher discharge current measured. A hump of  $n_e$  over an extended region between  $R = 4$  cm and  $R = 12$  cm can be observed at different  $Z$  positions. Meanwhile, the peak delay time was shorter in this region. The widened race track indeed spread out the coverage of the intense plasma but did not address the low plasma density at the center and the edge of the chamber.

The spiral magnetic field design included multiple turns of race tracks, covering the center as well as the outer edge. Figure 10(c) shows the peak  $n_e$  and the peak delay time using this design. The radial scanning orientation is marked by an arrow in figure 4(c). Right below the target ( $Z = 13$  cm), there are three  $n_e$  peaks resulting from the race tracks at  $R = 0$ , 8 and 13 cm. The distribution of the downstream plasma density quickly flattened. The density decrease near the edge was expected since the chamber wall served as a plasma sink. The distribution of the peak delay time was uniform from the center to  $R = 10$  cm on the substrate level. In short, the spiral magnet configuration obtained a plasma with superior uniformity, in

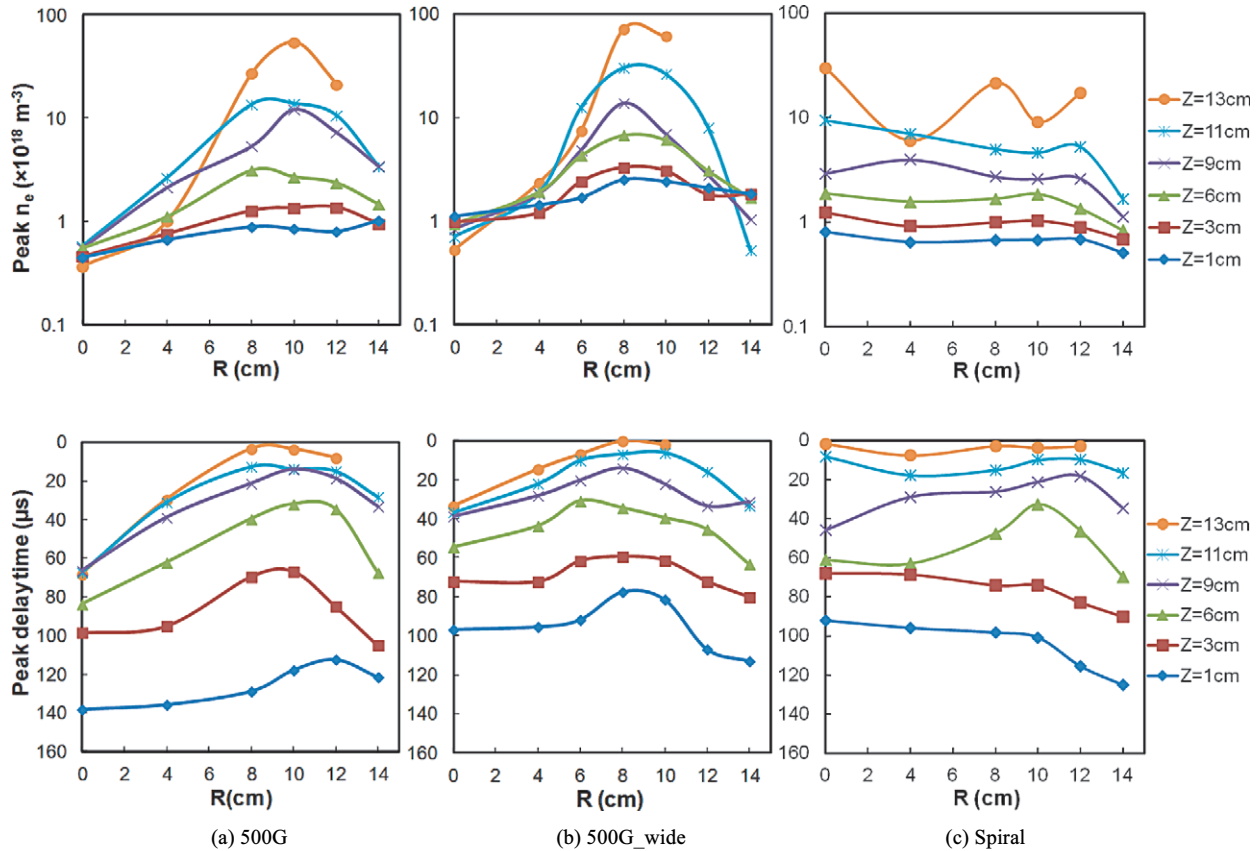


**Figure 10.** Peak  $n_e$  and the corresponding peak delay time of the plasma expansion in different configurations: (a) 500 G, (b) 500 G\_wide and (c) Spiral.

addition to its better target utilization. The design can be easily scaled up further for larger area depositions.

#### 4. Conclusions

Magnetic field configurations were shown to have some significant and unique effects on high-power impulse magnetron sputtering (HiPIMS), regarding the discharge characteristics, plasma behaviors and target utilization. A stronger magnetic field produced a higher discharge current and a denser plasma as a result of more efficient electron confinement. It also led to a faster plasma expansion from the race track region to the rest of the chamber after the pulse. The electric potential drop in the presheath and the bulk plasma region reduced to zero quickly in the 200 G configuration, but remained large for a longer period in the 800 G configuration so that the electron drifting was facilitated by a greater electric field. With increased magnetic field strength, the plasma expansion was observed to change from close to isotropic to more directional toward the substrate, which was likely due to the different electric field distributions and a stronger retardation of diffusion in the radial direction than in the axial direction.

The race track pattern was varied to optimize the target utilization and the downstream plasma uniformity. The configuration of wider race track generated a higher pulse current, and extended the intense plasma coverage on the

substrate. Attempts were made to spread the erosion evenly on the target, but the discharge currents were relatively low due to the non-closed race tracks. A closed path for electrons to drift along is still essential in HiPIMS. A spiral-shaped magnetic field configuration was able to generate a high pulse current, achieve a downstream plasma with superior uniformity, and yield a better target utilization even without the assistance of magnet rotation.

#### Acknowledgments

This study was supported by the Center for Lasers and Plasma in Advanced Manufacturing (National Science Foundation, Grant No CMMI09-53057). The authors would like to thank Dexter Magnetic Technologies for providing the magnetron pack, Huettinger Electronic for providing the pulsed plasma generator and Beckman Visualization Lab at the University of Illinois for COMSOL software access.

#### References

- [1] Kelly P J and Arnell R D 2000 *Vacuum* **56** 159
- [2] Helmersson U, Lattemann M, Bohlmark J, Ehlarsian A P and Gudmundsson J T 2006 *Thin Solid Films* **513** 1
- [3] Rosnagel S M 1999 *IBM J. Res. Dev.* **43** 163
- [4] Hopwood J 1998 *Phys. Plasmas* **5** 1624
- [5] Dulkan A, Ko E, Wu L, Karim I, Leaser K, Park K J, Meng L and Ruzic D N 2011 *J. Vac. Sci. Technol. A* **29** 041514

- [6] Yu H, Jiang Y, Wang T, Wu Z and Yu J and Wei X 2010 *J. Vac. Sci. Technol. A* **28** 466
- [7] Raju R, Meng L, Flauta R, Shin H, Neumann M J, Dockstader T A and Ruzic D N 2010 *Plasma Sources Sci. Technol. B* **19** 025011
- [8] Cheng P F, Rossnagel S M and Ruzic D N 1995 *J. Vac. Sci. Technol. B* **13** 203
- [9] Juliano D R, Ruzic D N, Allain M M C and Hayden D B 2002 *J. Appl. Phys.* **91** 605
- [10] Meng L, Raju R, Flauta R, Shin H, Ruzic D N and Hayden D B 2010 *J. Vac. Sci. Technol. A* **28** 112
- [11] Kouznetsov V, Macak K, Schneider J M, Helmersson U and Petrov I 1999 *Surf. Coat. Technol.* **122** 290
- [12] Alami J, Bolz S and Sarakinos K 2009 *J. Alloys Compounds* **483** 530
- [13] Bradley J W and Welzel T 2009 *J. Phys. D: Appl. Phys.* **42** 093001
- [14] Sarakinos K, Alami J and Konstantinidis S 2010 *Surf. Coat. Technol.* **204** 1661
- [15] Macak K, Kouznetzov V, Schneider J M, Helmersson U and Petrov I 2000 *J. Vac. Sci. Technol. A* **18** 1533
- [16] Bohlmark J, Alami J, Christou C, Ehasarian A P and Helmersson U 2005 *J. Vac. Sci. Technol. A* **23** 18
- [17] Mishra B, Moore J J, Lin J and Sproul W D 2010 *Mater. Sci. Forum* **638** 208
- [18] Rodil S E and Olaya J J 2006 *J. Phys.: Condens. Matter* **18** S1703
- [19] Zlatanovic M, Belosevac R and Kunosic A 1997 *Surf. Coat. Technol.* **90** 143
- [20] Ekpe S D, Jimenez F J, Field D J, Davis M J and Dew S K 2009 *J. Vac. Sci. Technol. A* **27** 1275
- [21] Bohlmark J, Helmersson U, VanZeeland M, Axnas I, Alami J and Brenning N 2004 *Plasma Sources Sci. Technol.* **13** 654
- [22] Lin J, Moore J J, Sproul W D and Lee S L 2011 *J. Vac. Sci. Technol. A* **29** 061301
- [23] Chen S and Goodings J M 1968 *J. Appl. Phys.* **39** 3300
- [24] Bryant P M, Voronin S A, Bradley J W and Vetushka A 2007 *J. Appl. Phys.* **102** 043302
- [25] Alami J, Gudmundsson J T, Bohlmark J, Birch J and Helmersson U 2005 *Plasma Sources Sci. Technol.* **14** 525
- [26] Meng L, Cloud A N, Jung S and Ruzic D N 2011 *J. Vac. Sci. Technol. A* **29** 011024
- [27] Pajdarova A D, Vlcek J, Kudlacek P and Lukas J 2009 *Plasma Sources Sci. Technol.* **18** 025008
- [28] Gudmundsson J T, Alami J and Helmersson U 2002 *Surf. Coat. Technol.* **161** 249
- [29] Seo S-H, In J-H and Chang H-Y 2005 *Plasma Sources Sci. Technol.* **14** 576
- [30] Bradley J W, Bäcker H, Kelly P J and Arnell R D 2001 *Surf. Coat. Technol.* **135** 221
- [31] Lieberman M A and Lichtenberg A J 1994 *Principles of Plasma Discharge and Materials Processing* (New York: Wiley)
- [32] Gudmundsson J T, Brenning N, Lundin D and Helmersson U 2012 *J. Vac. Sci. Technol. A* **30** 030801